

Full length article

Multicomponent γ' -strengthened Co-based superalloys with increased solvus temperatures and reduced mass densitiesEric A. Lass^{a,*}, Daniel J. Sauza^b, David C. Dunand^{b,c}, David N. Seidman^{b,c,d}^a Materials Science and Engineering Division, National Institute of Standards and Technology, 100 Bureau Drive, Gaithersburg, MD 20899-8555, USA^b Department of Materials Science and Engineering, Northwestern University, 2200 Campus Drive, Evanston, IL 60208-3108, USA^c NanoAl LLC, Illinois Science & Technology Park, 8025 Lamon Ave, Suite 446, Skokie, IL 60077, USA^d Northwestern University Center for Atom-Probe Tomography (NUCAPT), 2200 Campus Drive, Evanston, IL 60208-3108, USA

ARTICLE INFO

Article history:

Received 12 December 2017

Received in revised form

4 January 2018

Accepted 14 January 2018

Available online 3 February 2018

Keywords:

Co-based

Superalloy

Microstructural evolution

Alloy development

ABSTRACT

Several Co-Al-(W)-based γ -(FCC)/ γ' -(L1₂) alloys are investigated to combine recent results indicating significant increases in the γ' -solvus temperature with additions of Ni, Ta, and Ti, and reduced mass density with the substitution of Mo and Nb for W. A maximum solvus temperature of $1167 \pm 6^\circ\text{C}$ is achieved for an alloy with the composition Co-30Ni-7Al-4Ti-7W-1Ta (mole fraction $\times 100$); while the composition Co-30Ni-7Al-4Ti-3Mo-2W-1Nb-1Ta (L19) exhibits a promising combination of high γ' volume fraction and solvus temperature, low mass density, and excellent two-phase γ - γ' microstructural stability. Atom probe tomographic measurement of L19 aged for 4 h at 900°C indicates that Ni, Al, Ti, W, Nb, and Ta partition preferentially to the γ' -precipitates while Co partitions strongly to the γ -matrix. Molybdenum segregates at the γ/γ' interface, resulting in a reduction in the interfacial free energy of $1.63 \pm 0.85 \text{ mJ m}^{-2}$. Decreasing the mole fraction of Ni from 30% to 10% decreases the partitioning of Al and Ti to the γ' -phase and increases partitioning of Co, Mo, W, Nb, and Ta to the γ' -phase. From an analysis of coarsening kinetics (Ostwald ripening) at 900°C in Co- x Ni-7Al-4Ti-3Mo-2W-1Nb-1Ta ($x = 10$ and 30) interfacial free energies of $35.0 \pm 18.6 \text{ mJ m}^{-2}$ and $29.2 \pm 15.5 \text{ mJ m}^{-2}$ are calculated for mole fractions of Ni of 10% and 30%, respectively. This decrease in interfacial free energy with increasing Ni-concentration is attributed partially to both Mo-segregation at the γ - γ' interface and a decrease in the lattice parameter misfit between the γ' -precipitate and γ -matrix, and concomitantly the misfit strain energy.

© 2018 Acta Materialia Inc. Published by Elsevier Ltd. All rights reserved.

1. Introduction

Originally reported in 1973 [1], two-phase alloys within the ternary Co-Al-W system, consisting of an FCC (γ) matrix strengthened by coherent L1₂-ordered precipitates (γ'), analogous to Ni-based superalloys utilized for high temperature gas turbine applications, have attracted much attention since subsequently being reported in *Science* in 2006 [2]. This new class of precipitation-strengthened Co-based materials possesses higher solidus and liquidus temperatures and exhibit less segregation during solidification compared to traditional Ni-based superalloys [3]. Thus, significant research efforts are being focused on developing Co-based γ' -strengthened alloys for potentially supplanting Ni-based

superalloys. Although the flow stress and creep properties of Co-based alloys with three to five components are comparable to first- and second-generation Ni-based superalloys at temperature approaching 900°C [2,3], there are several issues needing to be addressed for these alloys to become practical engineering materials. These include: (i) a lower γ' solvus temperature compared to their Ni-based counterparts [2,3]; (ii) increased mass density as a result of the large amounts of W required to stabilize the γ' -phase; (iii) a decreased strength and yield stress anomaly exhibited by the Co₃(Al,W) L1₂ phase compared to Ni₃(Al,Ti) [4,5]; and (iv) resistance to oxidation and corrosion [6,7].

Recently, significant advances in two of these areas have been reported. It has been demonstrated that adding Ta and Ti to Co-Al-

* Corresponding author.

E-mail address: eric.lass@nist.gov (E.A. Lass).

W increases significantly the γ' solvus temperature, $T_{\gamma'}$. For example, the alloy Co-7Al-8W-4Ti-1Ta (by mole fraction¹) was shown to possess a $T_{\gamma'}$ of 1131 °C [8,9]. Adding Ni further increases the $T_{\gamma'}$, demonstrated by the recent reports of $T_{\gamma'}$ of 1182 °C in the alloy Co-29.6Ni-11.2Al-6.5W-2.8Ta [10] and of 1185 °C in the alloy Co-20Ni-7Al-7W-4Ti-2Ta [11]. Lass recently demonstrated the use of computational thermodynamics in designing the alloy Co-30Ni-9Al-3Ti-7W-2Ta-0.1B with an experimentally determined $T_{\gamma'}$ of 1218 °C, and a $T_{\gamma'}$ in excess of 1260 °C for other alloy compositions [12]. Pyczak et al. demonstrated that increasing the W-content increases the γ' solvus temperature by about 20 °C per 1% increase in W, while increasing the γ' volume fraction, $\phi_{\gamma'}$, thereby improving creep strength [13]. Tungsten additions, however, adversely affect the bulk alloy mass density, a critical design criterion for aerospace applications.

Makineni et al. recently reported Co-based γ - γ' alloys with decreased mass densities, achieved by replacing W with Mo and Nb [14], or Mo and Ta [15]. Quaternary W-free Co-10Al-5Mo-2Nb has a mass density of 8.38 g cm⁻³, comparable to the mass density of Ni-based superalloys, 8.5 g cm⁻³ to 9.0 g cm⁻³, and much lower than ternary Co-Al-W alloys; e.g., 9.82 g cm⁻³ for Co-9Al-9.8W [14,15]. Unfortunately, the γ' solvus temperatures of these W-free alloys are significantly lower than those of Co-Al-W-based alloys. Recent work has also focused on alloying Co-based superalloys with 10%–35% Ni, which improves γ' stability and increases its solvus temperature [14,16–18]. The present research combines the enhanced γ' stability provided by Ni, Ta, and Ti, with the decreased mass density of W-free alloys to create hybrid alloys with benefits of both above families.

2. Experimental procedures

A series of eight alloys was produced, whose compositions are provided in Table 1. The alloys can be divided into four sets of two compositions. Each set contains one alloy with 10% Ni and one with 30% Ni, and identical concentrations of the remaining alloying elements. The first two alloys (L12 and L13) add Ni to an alloy with a very similar composition to those reported by Xue et al. [8,9]. The second set (L14 and L15) adds Ti to a W-free alloy like those reported by Makineni et al. [14]. The final four alloys were generated by altering the compositions of L14 and L15 by first replacing 1% Nb with 1% Ta (L16 and L17) and then replacing 2% Mo with 2% W (and 1% Nb with 1% Ta) (L18 and L19). All alloys were prepared by arc melting under an Ar atmosphere the appropriate amounts of the pure elements to produce 50 g ingots. To compensate for the loss of Al due to evaporation during the melting process, the required mass of Al was increased by a factor of 1.05. Arc melting was performed by first melting all elements except Al and Ti together, flipping the ingot and remelting at least four times. The Al and Ti charges were then added and the ingot was remelted and flipped an additional four or five times.

Once cast, the ingots were homogenized at 1250 °C for 24 h in Ar-backfilled quartz ampules, followed by water quenching. Portions of each alloy were cut and subsequently aged at 900 °C for times ranging from 4 h to 1000 h, metallographically prepared using standard techniques, and etched via immersion in Carapella's reagent (96 mL ethanol, 2 mL hydrochloric acid, and 5 g ferric chloride) for about 5 s. Portions of the homogenized alloys were analyzed via differential scanning calorimetry (DSC) using a

Table 1

Alloy compositions and solvus, solidus and liquidus temperatures for the alloys investigated in the present work. Temperatures are in degrees Celsius and concentrations (nominal) are in mole fraction $\times 100$. Uncertainty in solvus temperature and density are twice the standard deviation of the measurements, or about a 95% confidence interval. One measurement of the solidus and liquidus temperatures were made, so no uncertainty is available, though experience indicates ± 10 °C should be at least a 95% confidence interval.

Alloy	Co	Ni	Al	Ti	W	Mo	Nb	Ta	Solvus	Solidus	Liquidus
L12	71	10	7	4	7	—	—	1	1134 \pm 4	1351	1413
L13	51	30	7	4	7	—	—	1	1167 \pm 6	1366	1419
L14	72	10	7	4	—	5	2	—	1021 \pm 6	1277	1360
L15	52	30	7	4	—	5	2	—	1082 \pm 2	1301	1353
L16	72	10	7	4	—	5	1	1	1033 \pm 8	1294	1367
L17	52	30	7	4	—	5	1	1	1105 \pm 2	1314	1367
L18	72	10	7	4	2	3	1	1	1076 \pm 4	1300	1377
L19	52	30	7	4	2	3	1	1	1126 \pm 2	1317	1385

heating rate of 10 K min⁻¹ under a flowing Ar environment at a flow rate of 20 mL min⁻¹. The mass density of each alloy was determined employing Archimedes' principle using water displacement. Microstructural investigation and compositional analysis was performed using a scanning electron microscope (SEM) equipped with energy dispersive x-ray spectroscopy (EDS). A grid-based manual point counting technique was used on representative backscatter electron (BSE) micrographs, using between 300 and 400 points per image, to estimate the γ' volume fraction. Precipitate size was determined by measuring the cube edge lengths in each perpendicular direction for between 20 and 100 individual γ' -precipitates for each annealing condition, then converting the average cube length, d , to equivalent precipitate radius, R , where $R^3 = 3d^3/(4\pi)$. X-ray diffraction (XRD) was performed for phase identification. XRD was also used to estimate the room-temperature γ and γ' lattice parameters and lattice parameter misfit using a least squares fit of two pseudo-Voigt peaks to each diffraction peak doublet visible in the XRD patterns for each sample. Vickers microhardness measurements were performed to evaluate the mechanical behavior of the alloys and its evolution with aging time.

One alloy of particular interest, L19, was chosen for further investigation as it exhibited a desirable combination of a high γ' solvus temperature, low mass density, and excellent microstructural stability. Samples of L19 were annealed at 900 °C for additional times of 15 min and 1 h to probe the early stages of γ' formation and coarsening, as well as at 1000 °C for 168 h and 1000 h and at 1100 °C for 168 h to investigate higher temperature microstructural stability. Atom-probe tomography (APT) was performed on a L19 specimen (aged at 900 °C for 4 h and brine-quenched) to determine the elemental compositions of the γ' -precipitates and γ -matrix, and the partitioning behavior, quantified using the partitioning coefficient, $K_i^{\gamma'/\gamma}$ defined as $C_i^{\gamma'}/C_i^{\gamma}$ (where $C_i^{\gamma'}$ is the mole fraction of species i in the γ' -precipitate and C_i^{γ} is the mole fraction of i in the γ -matrix). A sample of alloy L18 aged at 900 °C for 4 h was also investigated utilizing APT to explore the effects of the Ni-concentration on partitioning behavior. APT experiments were conducted using a LEAP² 4000X Si tomograph employing an ultraviolet (wavelength of 355 nm) pulsed picosecond laser, using a pulse energy of 20 pJ, a specimen base temperature of 25 \pm 1 K, a detection rate of 0.05 ions per pulse, and a pulse repetition rate of 500 kHz. The APT data were analyzed using the IVAS 3.6.12 software package (Cameca, Madison, WI). Quantitative identification and measurements of the γ' -precipitates and

¹ The alloy compositions throughout the text are designated by mole fraction of alloying elements ($\times 100$), with a balance of Co. For example, an alloy Co-7Al-7W contains a mole fraction of Al of 7%, a mole fraction of W of 7%, and a balance of Co, while an alloy with 50% Co contains a mole fraction of Co of 50%.

² Mention of commercial products does not imply endorsement by NIST, nor does it imply that such products or services are necessarily the best available for the purpose.

γ -matrix were performed using the envelope [19,20] and proximity histogram [21,22] methodologies. The OriginPro software package was used to perform the regression analysis of the experimental coarsening data for alloys L18 and L19. The regression analysis was performed by minimizing a weighted residual sum of squares, $\sum \{[R_i - R(t_i)]/R_i\}^2$, where R_i is the experimentally measured equivalent precipitate radius at time, t_i , and $R_i(t_i)$ is the model predicted equivalent radius at t_i . The weighting by $1/R_i$ was performed so that the residuals of each data point were expressed as a fraction of the measured value, rather than an absolute magnitude (i.e. a residual of 10 nm is more meaningful for $R_i = 30$ nm than for $R_i = 300$ nm).

3. Results and discussion

3.1. Mass density and γ' solvus temperature

The trends in alloy densities with composition, Table 2, are as anticipated from the compositions of the constituent elements. Alloys L12 and L13, which contain W and Ta but no Mo or Nb, are the densest at ≈ 9.5 g cm $^{-3}$, while L14 and L15, which contain only Mo and Nb but no W or Ta, are the least dense at ≈ 8.4 g cm $^{-3}$. When Nb and Mo are replaced with Ta and W, respectively, the mass density increases. The mass densities are about 8.6 g cm $^{-3}$ and 8.9 g cm $^{-3}$ for the L16/L17 and L18/L19 pairs, respectively. Also presented in Table 2 are the XRD determined lattice parameters for the γ and γ' phase, the resulting lattice parameter misfit, and the estimated alloy mass density, using the XRD determined lattice parameters to calculate the molar volume of each phase and the γ' volume fraction determined using SEM image analysis. Although the lattice parameters determined via XRD are not quantitatively accurate, the calculated densities are in good agreement with those determined by Archimedes' principle, and the lattice parameter misfits are small and positive, and similar to those measured for other Co-based superalloys [2,13]. A recent neutron diffraction investigation of an alloy with a similar composition to L19 reported a lattice parameter misfit of about 0.5% [23], slightly higher but in good agreement to the value 0.36% found here. More detailed, neutron- or synchrotron-based diffraction methods are required to accurately quantify the lattice parameters and lattice parameter mismatches of the other alloys.

The composition dependence of the γ' solvus temperature (Table 1) exhibits the same trend as for mass density. The densest alloys L12 and L13, containing the higher melting point elements Ta and W, possess the highest $T_{\gamma'}$, 1134 ± 4 °C and 1167 ± 6 °C, respectively, while the least dense alloys L14 and L15, with the lower melting point elements Nb and Mo, have the lowest $T_{\gamma'}$, 1021 ± 6 °C and 1082 ± 2 °C, respectively. Increasing the mole fraction of Ni from 10% to 30% increases the solvus temperature by

between about 30 °C (L12 to L13) and 70 °C (L16 to L17). Interestingly, replacing Mo with W is about twice as effective at increasing the γ' solvus temperature in the 10% Ni alloy series compared to the 30% Ni alloys. In contrast, replacing Nb with Ta is twice as effective in the 30% Ni alloys. The substitution of 2% W for Mo increases the γ' solvus by 43 °C from L16 to L18, but only by 21 °C from L17 to L19; while replacing 1% Nb with Ta increases the γ' solvus temperature by 12 °C in the 10Ni alloys (L14 to L16) and 25 °C in the 30Ni alloys (L15 to L17). The solidus and liquidus temperatures tend to increase as the amount of Mo+Nb is reduced, illustrated by comparing L14, L16, and L18, (or L15, L17, and L19) with Mo+Nb concentrations of 7%, 6%, and 4%, respectively.

3.2. Microstructure and microhardness

Fig. 1 presents the microstructures of the eight alloys after aging at 900 °C for 1000 h and water quenching. Alloys L12 and L13, without Mo or Nb, consist of a nearly 100% $\gamma+\gamma'$ two-phase microconstituent, except for regions along grain boundaries, which cracked prior to aging (not shown), most likely during quenching from the homogenization temperature. Along these cracks, Al is lost by evaporation during aging, resulting in regions where Al-poor phases readily form. EDS measurements on these precipitates reveal they are enriched in Ta, Ti, and W in alloys L12 and L13, as well as Mo and Nb in alloys L14–L18. The total mole fraction of Co+Ni in the precipitate phase is $\sim 76\%$, suggesting an A_3B type intermetallic phase. The XRD results in Fig. 2a indicate that besides the γ and γ' peaks, the only other observable peaks correspond to the A_3B -D0 $_{19}$, χ -phase, observed in the L13 and L18 alloys after aging at 900 °C for 1000 h. Additional weak χ -phase peaks are also present in the scans of alloys L12 through L18; however, their intensities are too low to observe in Fig. 2a. In alloys with little or no W, the χ -phase is enriched in Mo, Nb, Ta, and Ti, as determined by EDS analysis. This is not surprising since the χ -phase occurs in the equilibrium binary Co-Mo (Co $_3$ Mo) phase diagram, and has some solubility of Nb in the ternary Co-Mo-Nb system and significant solubility of Ti in the ternary Co-Mo-Ti system, primarily replacing Mo on the B sublattice [24]. The χ -phase is also observed along grain boundaries (GBs), cracked or intact, of alloys L14–L18, Fig. 1. Additionally, thin plates or rods of a secondary phase are observed forming within the $\gamma+\gamma'$ grain interiors in alloys L14 and L15. These plates are too small for semi-quantitative EDS analysis, which, however, reveals that they are enriched in Mo, Nb, and Ti. These precipitates are also likely χ -phase, which were observed by Makineni et al. in a Co-(30Ni)-10Al-5Mo-2Nb alloy [25]. A small amount of B2 is also found along the GBs of L14 near χ -precipitates, identified in Fig. 3c. There is some rafting of the γ' -precipitates, particularly in alloys L14 and L16, which may be the result of aging under internal stresses created by quenching following the

Table 2
The volume fraction calculated using a grid method on SEM micrographs (parentheses are APT calculated); density as calculated via XRD using the γ and γ' volume fractions and lattice parameters and as measured using Archimedes' method; and the room temperature γ and γ' lattice parameters and resulting room temperature lattice misfit δ , for each of the eight alloys in the present study. An approximate 95% confidence interval for the grid-determined volume fractions is $\pm 10\%$.

Alloy	$\phi_{\gamma'}$	Density, g cm $^{-3}$		$a-\gamma$, Å	$a-\gamma'$, Å	δ , $\times 100$
		Archimedes'	XRD			
L12	0.74	9.45 \pm 0.02	9.45 \pm 0.28	3.599 \pm 0.019	3.582 \pm 0.036	0.48
L13	0.75	9.49 \pm 0.04	9.58 \pm 0.22	3.581 \pm 0.015	3.575 \pm 0.029	0.16
L14	0.47	8.45 \pm 0.04	8.45 \pm 0.16	3.584 \pm 0.014	3.592 \pm 0.012	0.23
L15	0.63	8.42 \pm 0.08	8.49 \pm 0.32	3.575 \pm 0.015	3.583 \pm 0.026	0.22
L16	0.57	8.62 \pm 0.02	8.58 \pm 0.10	3.582 \pm 0.013	3.590 \pm 0.010	0.20
L17	0.60	8.57 \pm 0.06	8.47 \pm 0.10	3.583 \pm 0.018	3.613 \pm 0.013	0.86
L18	0.68 (0.78 \pm 0.04)	8.85 \pm 0.08	8.81 \pm 0.10	3.576 \pm 0.005	3.597 \pm 0.002	0.59
L19	0.65 (0.61 \pm 0.02)	8.89 \pm 0.02	8.84 \pm 0.18	3.577 \pm 0.009	3.590 \pm 0.014	0.36

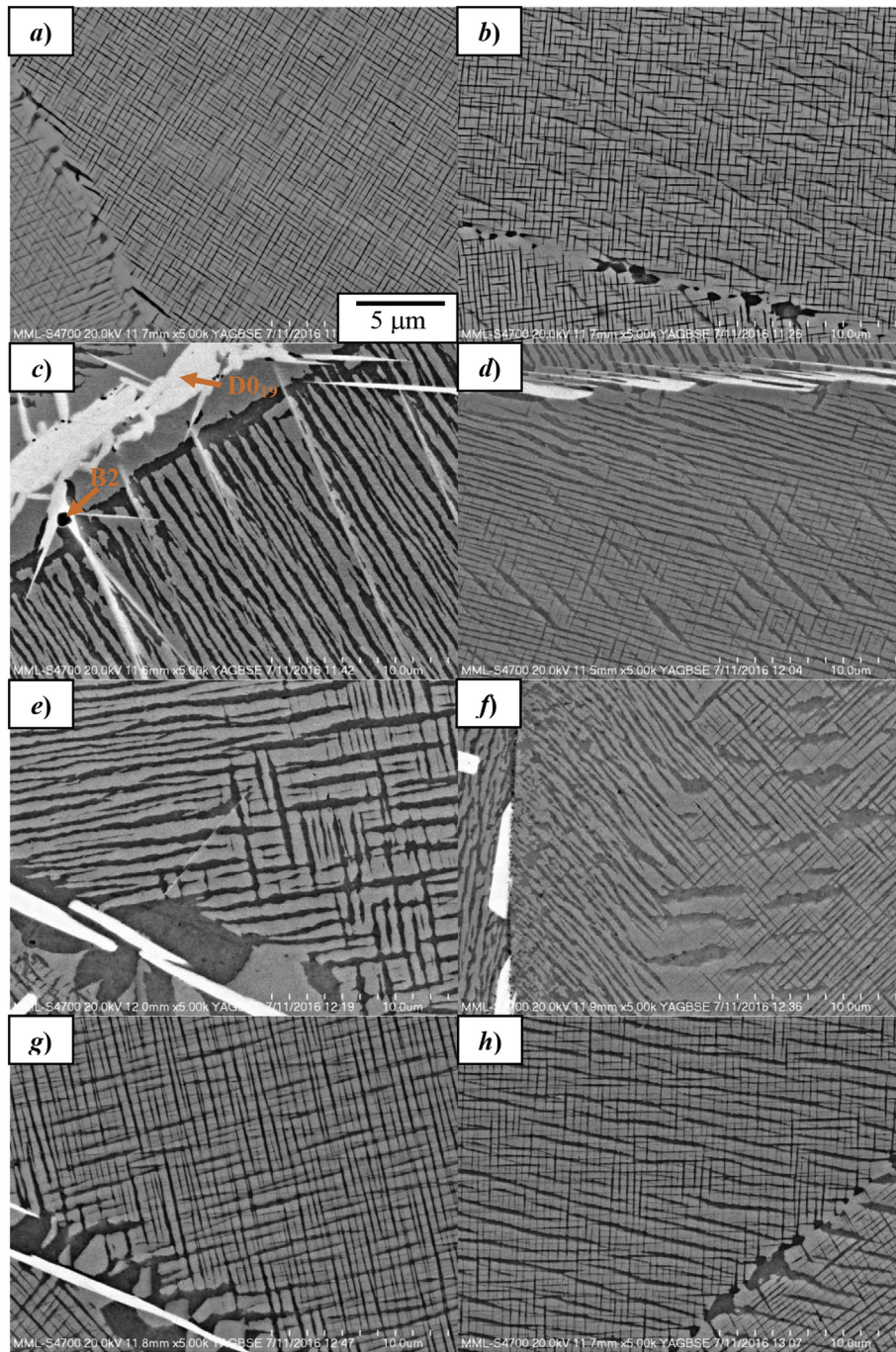


Fig. 1. SEM micrographs of eight alloys, L12 through L19, a) through h), respectively, after annealing at 900 °C for 1000 h and water quenching. The dark and light gray phases are γ and γ' , respectively; while the brightest phase, located at the grain boundaries is $D0_{19}$. The small black precipitates in L14 (arrows) are B2. The scale bar in a is representative for all images.

homogenization step.

The evolution of the Vickers microhardness with aging time at 900 °C is presented in Fig. 2b. The microhardness values of L12 and L13 continue to increase through 1000 h, suggesting that the alloys have not yet achieved peak aging conditions. Conversely, in alloys L14, L15, and L16, the microhardness peaks at 4 h, and steadily decreases with increasing aging time, indicating that the peak aging time is a few hours. The microhardness of L17, L18 and L19 peaks after 4 h, then decreases with increasing aging time to 168 h. The microhardness then appears to increase again after 1000 h at

900 °C in these three alloys. The measurement uncertainties (expressed as twice the standard deviation of the measurements, or approximately a 95% confidence interval) overlap for the microhardness values at 168 h and 1000 h, so it is unclear whether the apparent increase is statistically significant. If real, this peculiar behavior is certainly worthy of further investigation. However, it is outside the scope of the present work, and will be the subject of a future report.

Of the eight alloys, L19 stands out as the only one where no secondary phases are observed in the microstructure after aging for

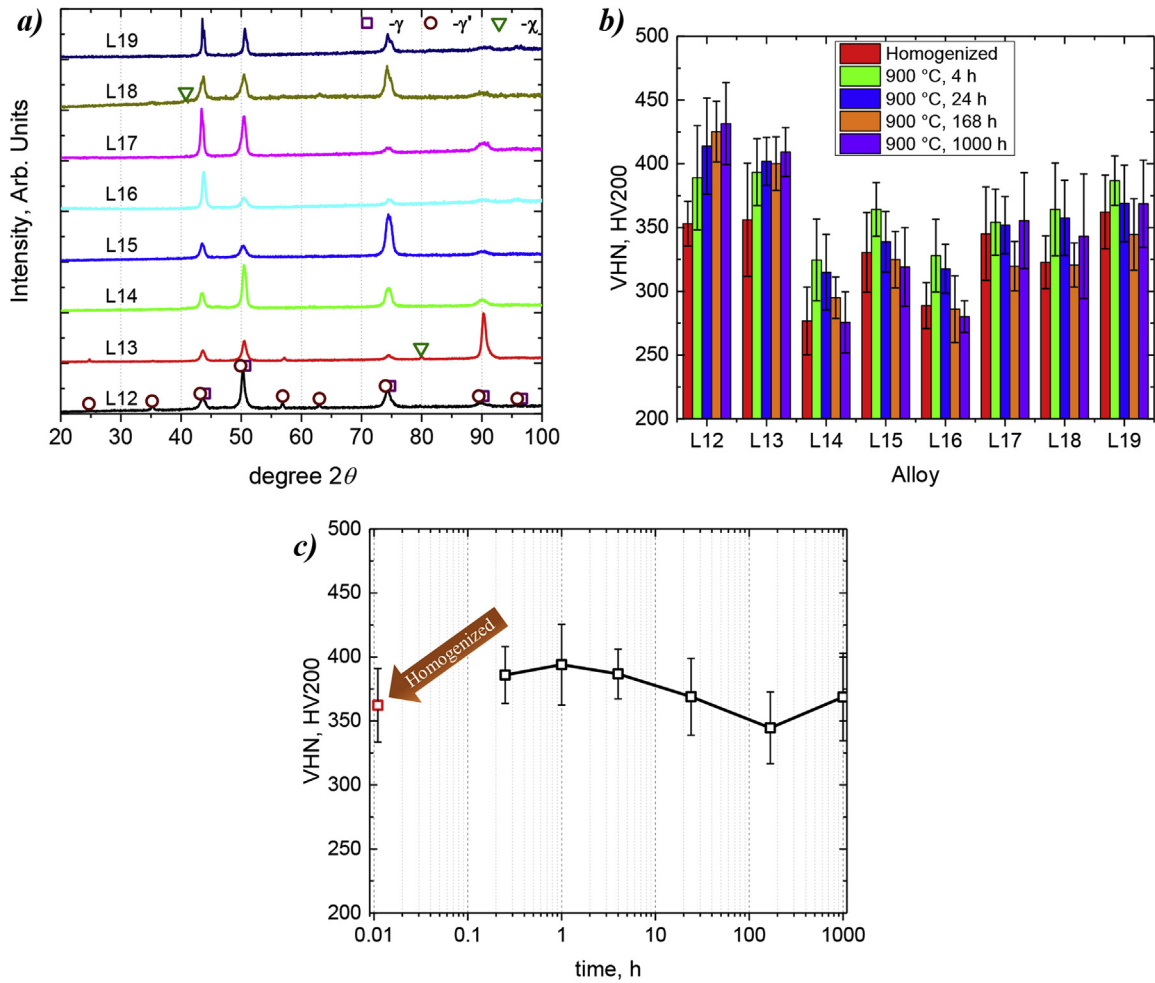


Fig. 2. a) X-ray diffraction patterns of the eight alloys after annealing at 900 °C for 1000 h showing primarily γ and γ' peaks in all alloys. Small peaks corresponding to the $D0_{19}$, χ -phase are visible in L13 and L18 (triangles); b) Vickers microhardness of each alloy as a function of annealing time at 900 °C; and c) the Vickers microhardness of L19 annealed at 900 °C for 15 min to 1000 h.

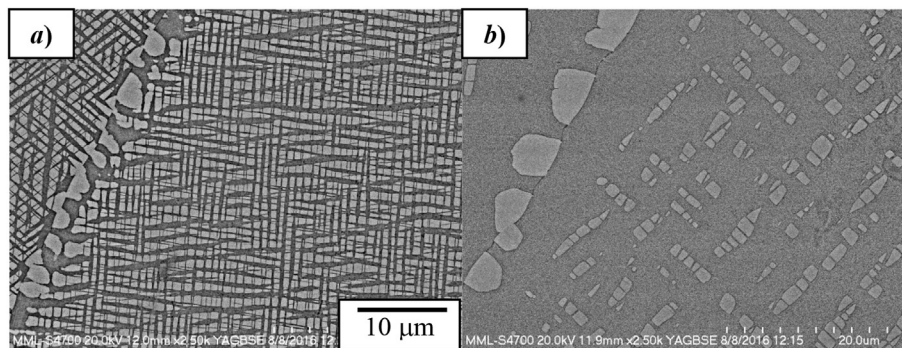


Fig. 3. SEM micrographs of L19 annealed for 168 h at a) 1000 °C and b) 1100 °C showing a γ - γ' microstructure with no secondary phases. The precipitates at the grain boundaries are coarsened γ' . The scale bar in a is representative for all images.

1000 h at 900 °C. A more detailed investigation of the early aging times of L19 indicates a peak aging time of 1 h at 900 °C, shown in Fig. 2c. Additionally, no secondary phase formation is observed in L19 after aging for 168 h at 1000 °C or 1100 °C, shown in the micrographs of Fig. 3, which also illustrate the coarsening of the γ' -precipitates in the grain interiors and at GBs. The γ' solvus temperature of L19 is quite high, 1126 ± 2 °C, and it displays a mass

density $< 9 \text{ g cm}^{-3}$, making it an interesting candidate for further investigation.

3.3. Atom-probe tomography of L18 and L19

Fig. 4a displays a 3-D APT reconstruction of alloy L19 aged for 4 h at 900 °C and brine quenched. The 3-D reconstruction consists

of 6×10^7 atoms and contains several partial cuboidal γ' -precipitates bordered by γ -matrix channels, delineated by a 50% Co isoconcentration surface. The bulk nanotip concentrations, Table 3, display good agreement with the nominal alloy composition of Co-30Ni-7Al-4Ti-2W-3Mo-1Nb-1Ta. The partitioning coefficient, $K_i^{\gamma/\gamma'}$, is represented graphically by proximity histograms taken across the γ/γ' heterophase interface, Fig. 4a and c, and quantified by determining the far-field (*ff*) average concentration values away from the γ/γ' heterophase interface, Table 3. The error attributed to the concentration measurements is given by

$$\sigma = \sqrt{\frac{C_i(1 - C_i)}{N_T}} \quad (1)$$

where σ is the statistical counting uncertainty, C_i is the measured *ff* concentration of species *i*, and N_T is the total number of type *i* atoms collected in the sampled region.

Qualitatively, the partitioning behavior of the constituent elements of L19 can be described as an overlap of solute partitioning characteristics of Co-based and Ni-based alloys. Tantalum and Ti partition strongly to the γ' -precipitates: $K_{Ta}^{\gamma/\gamma'} = 4.88 \pm 0.14$ and $K_{Ti}^{\gamma/\gamma'} = 3.36 \pm 0.04$. These elements are strong γ' -formers in both the Ni_3Al -L1₂ and $Co_3(Al,W)$ -L1₂ phases [8,9,26]. By contrast, Al, Nb, W and Ni exhibit smaller partitioning coefficients: 2.02 ± 0.02 , 1.90 ± 0.03 , 1.76 ± 0.03 , and 1.39 ± 0.01 , respectively. $K_{Al}^{\gamma/\gamma'}$ in ternary Co-Al-W is about 1.1 at 900 °C [27,28], and increases with Ni additions due to the stability of Ni_3Al -L1₂ [29]. Conversely, $K_W^{\gamma/\gamma'}$ has a value between 2 and 3 in Co-Al-W at 900 °C [29–31], which typically acts as a γ -former in Ni-base superalloys [26]. The present alloy displays an intermediate value of $K_W^{\gamma/\gamma'}$ of 1.76. Cobalt partitions strongly to the γ -matrix, with $K_{Co}^{\gamma/\gamma'} = 0.66 \pm 0.01$; a result of Ni partitioning to γ' and the preference to form a more energetically favorable Ni_3Al -like L1₂ phase compared to $Co_3(Al,W)$.

Table 3

Bulk and phase compositions as measured by atom probe tomography and associated partitioning coefficients for alloy L19 annealed at 900 °C for 4 h. Compositions are expressed in mole fraction $\times 100$.

	Bulk (APT)	γ	γ'	$K_i^{\gamma/\gamma'}$
Co	50.53 \pm 0.02	63.50 \pm 0.07	41.91 \pm 0.09	0.66 \pm 0.01
Ni	29.76 \pm 0.01	24.21 \pm 0.06	33.55 \pm 0.09	1.39 \pm 0.01
Al	7.53 \pm 0.01	4.63 \pm 0.03	9.35 \pm 0.05	2.02 \pm 0.02
Ti	4.13 \pm 0.01	1.72 \pm 0.01	5.78 \pm 0.04	3.36 \pm 0.04
W	1.92 \pm 0.01	1.33 \pm 0.02	2.34 \pm 0.03	1.76 \pm 0.03
Mo	3.13 \pm 0.01	3.00 \pm 0.03	3.10 \pm 0.17	1.03 \pm 0.01
Nb	2.00 \pm 0.01	1.29 \pm 0.01	2.47 \pm 0.03	1.90 \pm 0.03
Ta	1.01 \pm 0.01	0.31 \pm 0.01	1.51 \pm 0.02	4.88 \pm 0.14

Interestingly, for L19, the partitioning ratio for Mo is near unity ($K_{Mo}^{\gamma/\gamma'} = 1.03 \pm 0.01$) indicating that Mo does not have a strong preference for either phase. This is consistent with Mo partitioning to the γ' -phase in Co-9Al-10W-3Mo [32], and to the γ phase in the Ni-containing multicomponent alloy Co-29Ni-6Cr-12Al-5W-2Mo-2Ta [33]. In the present Co-Ni based alloy, confined segregation of Mo is also observed at the γ/γ' interface, Fig. 5.

The Gibbsian interfacial excess, Γ_i , and change in the integral free energy, $\Delta\sigma_{\gamma/\gamma'}$ of the heterophase interface as a result of the observed Mo segregation, displayed in more detail in Fig. 5b, can be quantified using an integral methodology proposed by Blum et al. [34]. The local Gibbsian interfacial excess at every point along the concentration profile is then given by

$$d\Gamma_i = [C_i^m(x) - C_i^0(x)] dx \quad (2)$$

where C_i^m is the local measured concentration of component *i*, and C_i^0 is a reference concentration of component *i* that would be present at every point along the concentration profile if local

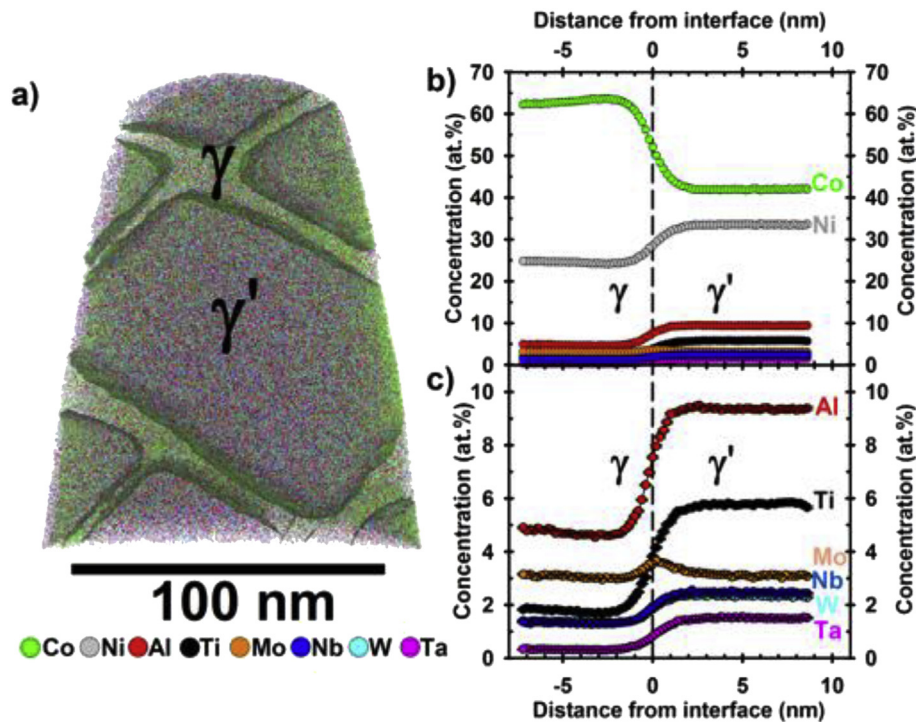


Fig. 4. a) 3D APT reconstruction of L19 aged for 4 h at 900 °C, revealing cuboidal primary γ' -precipitates (described by a 50% Co isoconcentration surface) separated by γ -matrix channels. (b) Concentration profiles generated from a proximity histogram of the constituent elements between the γ' -precipitates and the γ -matrix, where the zero position of the interface is defined as the inflection point of Co, the majority species. (c) Proximity histogram detailing the partitioning behavior of the minority species.

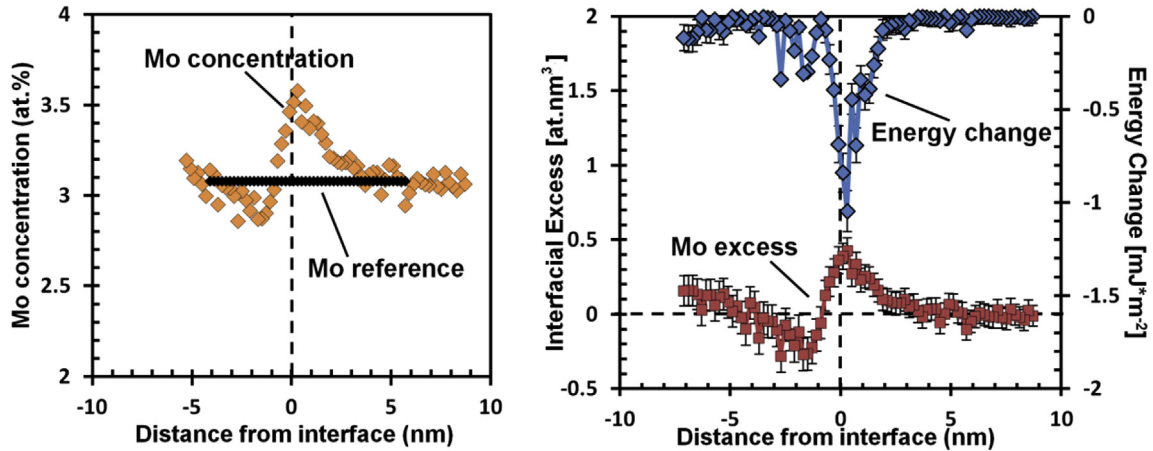


Fig. 5. (a) Concentration profile of Mo across the γ/γ' interface (orange) in Fig. 4, and reference concentration profile at 3.1% Mo (black). (b) Calculated Mo excess concentration profile and the concomitant decrease in the interfacial free energy due to segregation. (For interpretation of the references to colour in this figure legend, the reader is referred to the Web version of this article.)

segregation were not present at the interface. Because $K_{Mo}^{\gamma/\gamma'}$ is near unity, a horizontal line corresponding to a Mo concentration of 3.1% is used for C_i^0 . The corresponding local decrease in $\Delta\sigma_i$ is then calculated from

$$d\Delta\sigma_{\gamma/\gamma'} = -d\Gamma_i k_B T \ln \left(\frac{C_i^m(x)}{C_i^0(x)} \right) \quad (3)$$

where k_B is the Boltzmann constant and T is in Kelvin. For alloy L19 aged 4 h at 900 °C the calculated total Gibbsian interfacial excess is 0.43 ± 0.17 atoms \cdot nm $^{-3} \cdot$ m $^{-2}$ and a corresponding reduction in the interfacial free energy 1.63 ± 0.85 mJ m $^{-2}$. The modest depletion of Mo on the left-hand side of the interface, Fig. 5a, is most likely a transient kinetic effect because of the system not yet achieving local equilibrium after 4 h aging at 900 °C. This phenomenon has been previously observed for APT investigations of model Ni–Al–Cr alloys [35,36].

The volume fraction of γ' , $\phi_{\gamma'}$, determined from the experimentally-measured γ -matrix and γ' -precipitate concentrations, is given by the mass balance equation

$$\phi_{\gamma'} = \left(C_i^{bulk} - C_i^{\gamma} \right) / \left(C_i^{\gamma'} - C_i^{\gamma} \right) \quad (4)$$

where C_i^{bulk} is the bulk nanotip concentration measured experimentally utilizing APT. From Table 3, $\phi_{\gamma'} = 60.8 \pm 0.06\%$ for L19 aged 4 h at 900 °C. The error, given by the error of the linear regression is small indicating good agreement among the concentrations measured employing APT for each phase and for the bulk nanotip. The value is also in agreement with the value of $65 \pm 10\%$ determined utilizing microstructural analysis, Table 2.

Fig. 6 shows a top-down view of an APT reconstruction of alloy L18 aged for 4 h at 900 °C and brine-quenched. The 3-D reconstruction consists of 3×10^6 atoms and contains several partial γ' -precipitates separated by γ -matrix channels, described by a 70% Co isoconcentration surface. The bulk elemental concentrations measured by APT show reasonable agreement with the nominal composition, Table 4. The partitioning tendencies of the constituent elements to either side of the γ/γ' heterophase interface in alloy L18, Fig. 6b and c, are qualitatively similar to those measured for alloy L19 with higher Ni concentration, Fig. 4b and c, with the notable exception of Mo which convincingly partitions to the γ' -precipitates in the lower Ni-content alloy L18. The effect of increasing the Ni content in the alloy from 10 to 30%, via replacing Co, on the

elemental partitioning coefficients in these alloys is illustrated graphically in Fig. 7. Alloy L19, with 30% Ni, demonstrates enhanced partitioning of Ti and Al to the γ' -precipitates, with a corresponding reduction in $K_i^{\gamma/\gamma'}$ for Ta, W, Nb, and Mo when compared to alloy L18 with 10% Ni. This is consistent with an increased Ni-like partitioning behavior and the strong propensity of Al and Ti to form Ni $_3$ (Al,Ti) with an L1 $_2$ structure, as described above.

3.4. Microstructural coarsening

Fig. 8 presents representative micrographs of the γ - γ' microstructure of alloy L19 after aging at 900 °C for times between 15 min and 168 h. It is evident that the γ' volume fraction achieves a relatively constant value of 60%–70% early during aging at 900 °C, after 15 min or earlier, Fig. 8a. Thus, the microstructural evolution of the L19 alloy at 900 °C consists of approximately stationary coarsening (Ostwald ripening) for all times investigated, and can be described by the LSW theory [37,38].

$$\langle R(t) \rangle^n - \langle R(t_0) \rangle^n = k(t - t_0) \quad (5)$$

where $R(t)$ is the mean precipitate radius at time t , $R(t_0)$ is the initial precipitate radius at $t = t_0$, the time at which stationary coarsening commences, k is the coarsening rate constant, and n is the temporal exponent. For volume diffusion-limited coarsening, which is often encountered, $n = 3$; while $n = 2$ when interface reaction is the rate limiting process. To determine the temporal exponent and coarsening rate constant for a given set of experimental data, i.e. $R(t)$ versus t , Eq. (5) is solved for $R(t)$

$$\begin{aligned} R(t) &= \left[\langle R(t_0) \rangle^n + k(t - t_0) \right]^{\frac{1}{n}} \\ &= \left\{ \left[\langle R(t_0) \rangle^n - kt_0 \right] + kt \right\}^{\frac{1}{n}} = (C_1 + kt)^{\frac{1}{n}} \end{aligned} \quad (6)$$

Examining Eq. (6), of the four unknown parameters, k , n , t_0 , and $R(t_0)$, $R(t_0)$ and t_0 cannot be determined independently, since for arbitrary values for k and n , there are infinite combinations of $R(t_0)$ and t_0 that would result in equivalent equations. Therefore, $R(t_0)$ and t_0 are combined into a single parameter C_1 , which is treated as a separate variable. Multivariate nonlinear regression analysis is then employed to determine the values of C_1 , k , and n that best fit the experimental data.

The measured equivalent precipitate radii of alloys L18 and L19 as a function of annealing time at 900 °C are presented in Table 5. Fig. 9a

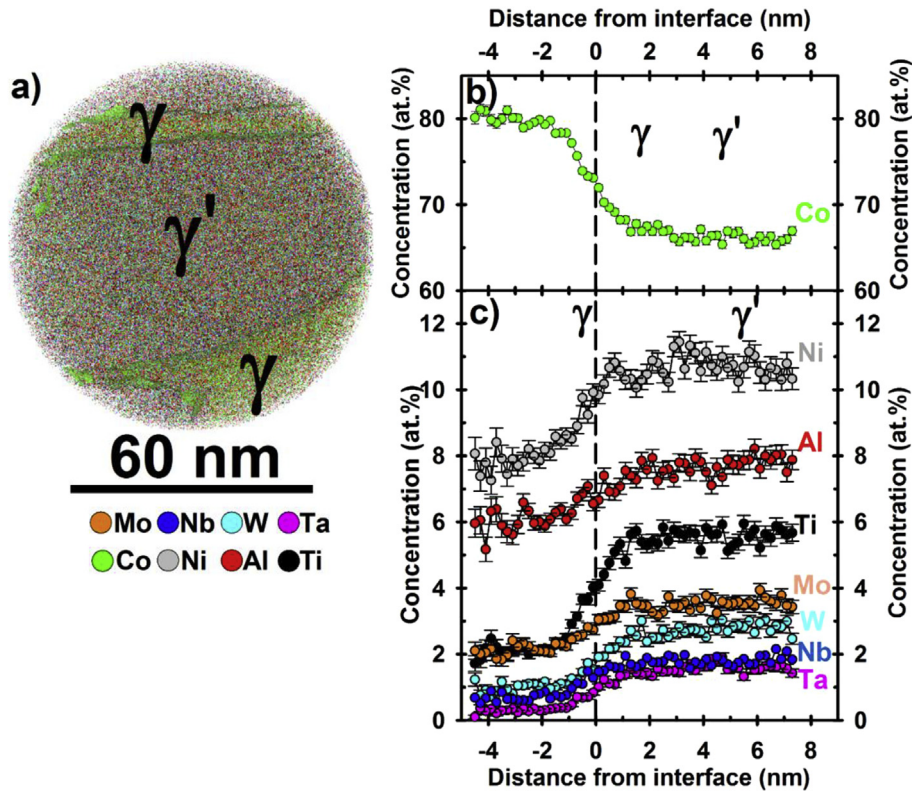


Fig. 6. a) 3D APT reconstruction of L18 aged for 4 h at 900 °C, revealing partial γ' -precipitates (described by a 70% Co isoconcentration surface) separated by γ -matrix channels. Concentration profiles of b) Co and c) the minority species between the γ' -precipitates and γ -matrix, where the zero position of the interface is defined as the inflection point of Co.

Table 4

Bulk and phase compositions as measured by atom probe tomography and associated partitioning coefficients for alloy L18 annealed at 900 °C for 4 h. Compositions are expressed in mole fraction $\times 100$.

	Bulk (APT)	γ	γ'	$K_{\gamma'/\gamma}^i$
Co	68.97 ± 0.07	79.79 ± 0.38	66.15 ± 0.49	0.83 ± 0.01
Ni	10.23 ± 0.02	7.96 ± 0.25	10.69 ± 0.32	1.34 ± 0.06
Al	7.39 ± 0.02	6.11 ± 0.23	7.73 ± 0.28	1.26 ± 0.07
Ti	4.86 ± 0.01	2.14 ± 0.14	5.55 ± 0.24	2.60 ± 0.20
W	2.37 ± 0.01	1.09 ± 0.10	2.87 ± 1.09	2.65 ± 0.29
Mo	3.25 ± 0.01	2.18 ± 0.14	3.57 ± 0.19	1.63 ± 0.14
Nb	1.61 ± 0.01	0.70 ± 0.08	1.79 ± 0.14	2.54 ± 0.34
Ta	1.29 ± 0.01	0.30 ± 0.05	1.63 ± 0.13	5.44 ± 1.03

and *b* presents the results of least squares regression analyses of the data for alloys L18 and L19, respectively. Both nonlinear and linearized (i.e. $n = 3$) are presented for both alloys. The optimized regression parameters, C_1 , k , and n for each regression are listed in Table 6, where the given uncertainties are the standard error calculated employing the regression analyses [39]. Nonlinear regression analysis yields temporal exponents for L18 and L19 of 2.870 ± 0.388 and 2.961 ± 0.334 , respectively. Both are very nearly $n = 3$, indicating that coarsening is diffusion-limited in both cases. For the case of L19, the coarsening rate constant is comparable for both nonlinear and linearized regression analyses, $11040 \pm 18710 \text{ nm}^3 \text{ h}^{-1}$ and $13480 \pm 1960 \text{ nm}^3 \text{ h}^{-1}$, respectively; while for L18 the coarsening rate constant calculated using nonlinear regression is about half that found using linearized regression analysis, $7080 \pm 14130 \text{ nm}^3 \text{ h}^{-1}$ and $13960 \pm 2080 \text{ nm}^3 \text{ h}^{-1}$, respectively. Note also that the standard error of the coarsening rate constant is significantly greater using nonlinear regression analysis because the inclusion of a fourth regression variable, n , adds a degree of freedom to the model and increases the uncertainty of the

optimized regression parameters [39].

For $n = 3$, i.e. the process is diffusion-limited, as demonstrated by the nonlinear regression analysis above, the coarsening rate constant can be related to thermodynamic and kinetic parameters. According to the LSW model

$$k_{LSW} = \frac{8D_i^\gamma C_i^{\gamma,\infty} V_m^\gamma \sigma_{\gamma/\gamma'}}{9N_a k_B T} \quad (7)$$

where D_i^γ is the diffusivity of component i in the γ -matrix, $\sigma_{\gamma/\gamma'}$ is the interfacial energy, V_m^γ the molar volume of the γ phase, and N_a Avagadro's number. While the classical LSW theory was developed using several simplifying assumptions, modifications have been made to account for finite precipitate volume fraction [40–42] and non-dilute systems [43]. However, the original LSW model and many of its extensions are valid strictly for binary, ideal solutions. Extending the treatments to multicomponent alloys introduces uncertainties, and requires the choice of component i which results in the slowest coarsening rate, that is, a rate limiting diffusional process. Several treatments of coarsening have been published that are extensions of the LSW model to ternary and higher order systems [44–46]. Recently, a generalized treatment of coarsening in multicomponent alloys was presented by Philippe and Voorhees (P-V) [47], which takes advantage of the increasingly available computational thermodynamic and diffusion data. In the limit $t \rightarrow \infty$, the P-V model yields a rate constant

$$k_{PV} = \frac{8V_m^\gamma \sigma_{\gamma/\gamma'}}{9(\Delta \bar{C})^T \mathbf{M}^{-1} \Delta \bar{C}} \quad (8)$$

where $\Delta \bar{C}$ and $(\Delta \bar{C})^T$ are the concentration and transposed

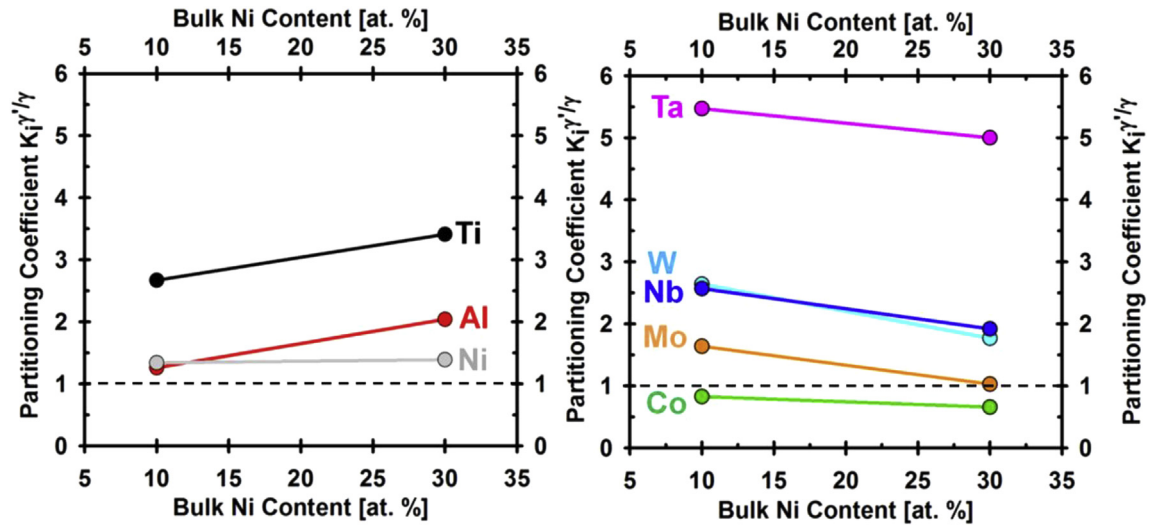


Fig. 7. Change in elemental partitioning coefficient $K_{\gamma'/\gamma}$ with bulk Ni content, measured by APT for alloys L18 (left-hand side) and L19 (right-hand side) aged at 900 °C for 4 h.

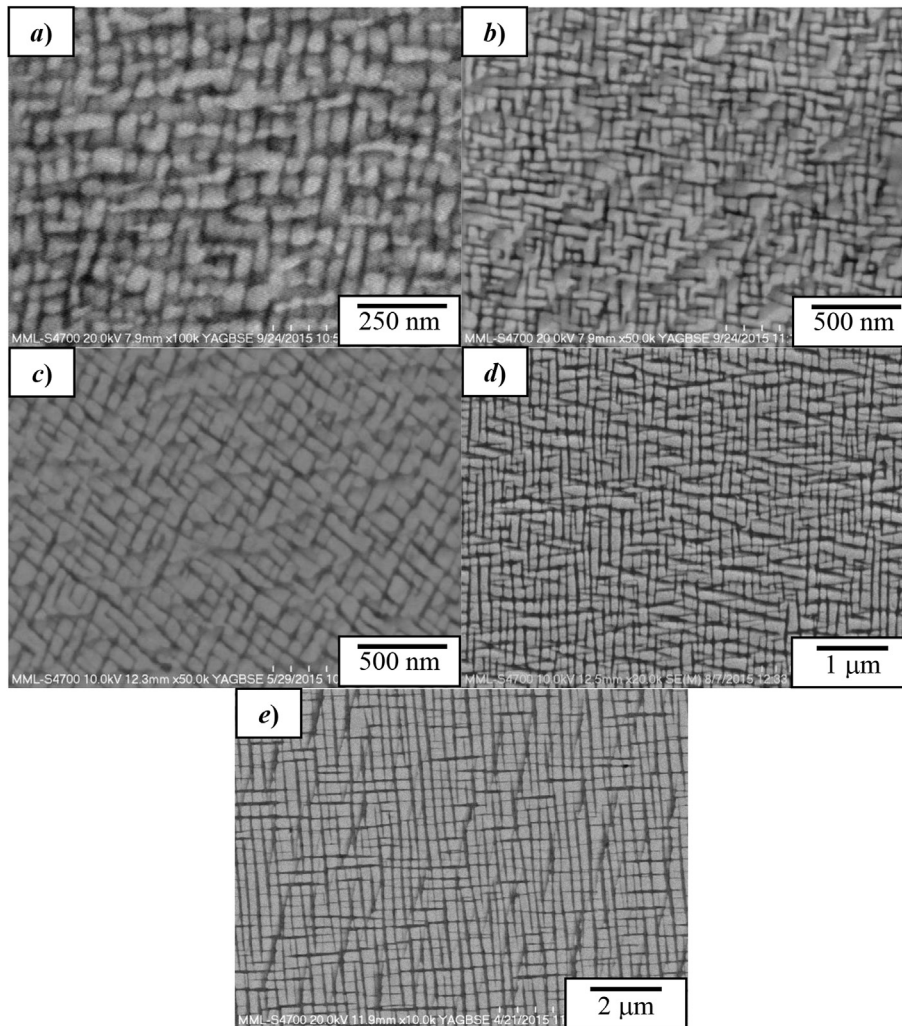


Fig. 8. Representative SEM micrographs of alloy L19 after annealing at 900 °C for a) 15 min, b) 1 h, c) 4 h, d) 24 h, and e) 168 h.

concentration vectors, i.e. the change in composition difference between γ' and γ , respectively, and \mathbf{M}^{-1} is the inverse of the

mobility matrix; defined by $\mathbf{D} = \mathbf{M}\mathbf{G}^{\gamma}$ with \mathbf{D} being the diffusivity matrix and \mathbf{G}^{γ} the Hessian of the Gibbs free energy of the γ -phase,

Table 5

Spherical equivalent precipitate radii as a function of annealing time for alloys L18 and L19 annealed at 900 °C.

t, h	R(t), nm	
	L18	L19
0.25	–	32.05 ± 14.68
1	–	35.95 ± 14.65
4	39.83 ± 21.28	46.86 ± 14.47
24	69.14 ± 31.29	66.46 ± 29.56
168	129.64 ± 72.77	134.46 ± 56.72
1000	244.83 ± 119.45	238.41 ± 73.93

that is $\mathbf{G}^\gamma = G_{\gamma,ij}$. When appropriate estimated values are known for V_m^γ , $\Delta\bar{C}$, and \mathbf{M}^{-1} , Eq. (8) can be used to determine $\sigma_{\gamma/\gamma'}$ from the coarsening rate constant determined from experimental data.

The room temperature value of V_m^γ of each alloy is estimated from the measured lattice parameters in Table 2 yielding $6.86 \times 10^{-6} \text{ m}^3 \text{ mol}^{-1}$ and $6.89 \times 10^{-6} \text{ m}^3 \text{ mol}^{-1}$ for alloys L18 and L19, respectively. Thermal expansion from room temperature to 900 °C is approximated using a rule-of-mixtures of the thermal expansion of the pure elements [48], yielding molar volumes of L18 and L19 at 900 °C of $7.13 \times 10^{-6} \text{ m}^3 \text{ mol}^{-1}$ and $7.19 \times 10^{-6} \text{ m}^3 \text{ mol}^{-1}$, respectively.

The appropriate atomic mobility parameters are calculated using the NIST Ni-based mobility database [49] and the Thermo-Calc/Dictra software package [50]. Because only mobility data are required in Eq. (8), no thermodynamic database is required. Several different Calphad mobility matrices exist, depending on the frame of reference and energy potential gradient being used to describe diffusion [51]. The P-V model uses a volume-fixed frame of reference. In the P-V model, $\mathbf{D} = \mathbf{M}\mathbf{G}^\gamma$, which relates the diffusivity matrix to the second derivatives of the molar free energy with

respect to concentrations, i.e., $\mathbf{G}^\gamma = G_{\gamma,ij} = \partial^2 G_\gamma / (\partial C_i \partial C_j)$. In terms of chemical potentials [46], $G_{\gamma,ij} = \mu_{i,j} - \mu_{n,j}$, where $\mu_{i,j}$ is the partial derivative of chemical potential of component i with respect to C_j , and component n is the one chosen as the dependent composition variable. With \mathbf{G}^γ the potential gradient of interest, the appropriate mobility term is the symmetric matrix L''_{ki} [51].

$$L''_{ki} = \sum_{j=1}^n \sum_{r=1}^n (\delta_{ir} - C_i) (\delta_{jk} - C_k) L_{jr} \quad (9)$$

where δ_{ij} is the Kronecker delta, i.e., 1 for $i=j$ and 0 otherwise, and $L_{ij} = \delta_{ij} C_i M_i$, where M_i is the composition-, temperature-, and pressure-dependent atomic mobility of component i described in the Calphad mobility database. Using the NIST Ni-mobility database, Tables 7 and 8 report the L''_{ki} matrices calculated at 900 °C for the γ' -matrix compositions (determined via APT) of L19 (Table 3) and L18 (Table 4), respectively.

The $\Delta\bar{C}$ are determined from the APT-measured concentrations (Tables 3 and 4 for L19 and L18, respectively), leaving $\sigma_{\gamma/\gamma'}$ as the only unknown parameter on the right-hand side of Eq. (8). Therefore, the interfacial free energy can be estimated from the experimentally determined coarsening rate constant, k . The calculated $\sigma_{\gamma/\gamma'}$ for L18 and L19, using the coarsening rate constants determined using both nonlinear and linearized regression analyses, are presented in Table 6. The $\sigma_{\gamma/\gamma'}$ (at 900 °C) calculated using the nonlinear regression analyzed coarsening rate constants are $23.9 \pm 42.4 \text{ mJ m}^{-2}$ and $17.7 \pm 36.6 \text{ mJ m}^{-2}$ for L19 and L18, respectively, where the uncertainties are expressed as the combined uncertainties of the parameters used in the calculation. The uncertainty in the atomic mobilities was estimated to be 50% of the calculated values, based on observed uncertainty in the diffusivity data [52,53]; while the uncertainty in molar volume was estimated

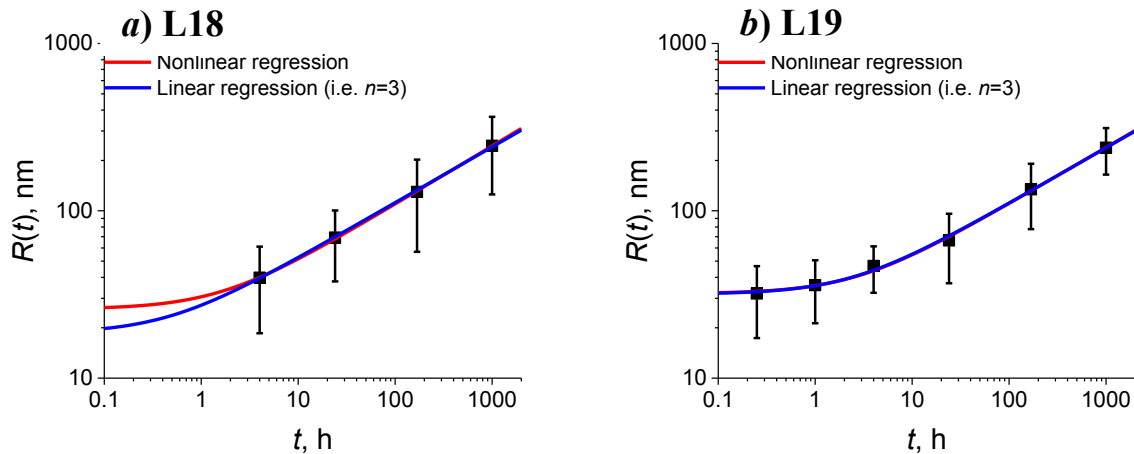


Fig. 9. Microstructural coarsening data and the calculated coarsening rate equations for a) L18 and b) L19, optimized using both nonlinear and linearized (i.e. $n=3$) weighted least squares regression analysis.

Table 6

Coarsening parameters, C_i , k , and n in Eq. (6) determined using both nonlinear and linear (with $n=3$) regression analysis of the experimental data in Table 5, along with the interfacial free energy calculated using the P-V model for each regression analysis.

	L18		L19	
	Nonlinear	$n=3$	Nonlinear	$n=3$
C_i (nm)	11300 ± 18800	6350 ± 31100	28650 ± 30090	32050 ± 13660
k ($\text{nm}^3 \text{ h}^{-1}$)	7080 ± 14130	13960 ± 2080	11040 ± 18710	13480 ± 1960
n	2.870 ± 0.388	3	2.961 ± 0.334	3
$\sigma_{\gamma/\gamma'}$ (mJ m^{-2})	17.7 ± 36.6	35.0 ± 18.6	23.9 ± 42.4	29.2 ± 15.5

Table 7
Mobility matrix, L_{ki}^{γ} , for alloy L19 calculated at 900 °C for the γ -matrix composition determined via APT (Table 3). Values are multiplied by 10^{23} , and the units are $\text{m}^2 \text{mol}^{-1} \text{s}^{-1}$.

$k \setminus i$	Al	Mo	Nb	Ni	Ta	Ti	W
Al	115.3	-3.378	-1.821	-27.10	-0.4206	-4.616	-1.362
Mo	-3.378	8.876	-0.2433	0.01359	-0.04748	-1.742	0.08327
Nb	-1.821	-0.2433	11.56	-1.919	-0.04506	-0.8859	-0.06992
Ni	-27.10	0.01359	-1.919	69.20	-0.3724	-14.00	0.7182
Ta	-0.4206	-0.04748	-0.04506	-0.3724	2.453	-0.2066	-0.01193
Ti	-4.616	-1.742	-0.8859	-14.00	-0.2066	60.96	-0.7218
W	-1.362	0.08327	-0.06992	0.7182	-0.01193	-0.7218	1.074

Table 8
Mobility matrix, L_{ki}^{γ} , for alloy L18 calculated at 900 °C for the γ -matrix composition determined via APT (Table 4). Values are multiplied by 10^{23} , and the units are $\text{m}^2 \text{mol}^{-1} \text{s}^{-1}$.

$k \setminus i$	Al	Mo	Nb	Ni	Ta	Ti	W
Al	221.4	-4.844	-1.693	-20.58	-0.7480	-9.571	-2.236
Mo	-4.844	7.814	-0.03704	-0.8928	-0.02380	-1.681	0.08551
Nb	-1.693	-0.03704	4.730	-0.4666	-0.01442	-0.5882	0.002819
Ni	-20.58	-0.8928	-0.4666	68.70	-0.2289	-7.152	-0.2038
Ta	-0.7480	-0.02380	-0.01442	-0.2289	2.395	-0.2599	-0.002750
Ti	-9.571	-1.681	-0.5882	-7.152	-0.2599	83.13	-0.7754
W	-2.236	0.08551	0.002819	-0.2038	-0.002750	-0.7754	0.9155

as 10% of the calculated molar volume. The uncertainties in the interfacial free energies are about twice the magnitude of $\sigma_{\gamma/\gamma'}$, arising primarily due to the combined uncertainties in atomic mobilities and coarsening rate constant.

For $n=3$, the calculated $\sigma_{\gamma/\gamma'}$ are $29.2 \pm 15.5 \text{ mJ m}^{-2}$ and $35.0 \pm 18.6 \text{ mJ m}^{-2}$ for L19 and L18, respectively. The uncertainties in these interfacial free energy values are a factor of 2–3 smaller than for the nonlinear regression analysis case, equal to approximately one half of the magnitude of $\sigma_{\gamma/\gamma'}$. This indicates that the uncertainty in the interfacial energy calculated using a linearized regression analysis with $n=3$ is primarily a result in the uncertainty in the atomic mobilities. The above nonlinear regression analyses demonstrate that $n \approx 3$ for both L18 and L19, indicating diffusion-limited coarsening behavior. Because diffusion-limited coarsening is known to follow an $n=3$ temporal exponent, the interfacial energies calculated after setting $n=3$ are valid and known for greater certainty than the nonlinear case. It is further noted that Eqs. (7) and (8) are meaningful only when n is exactly equal to three.

The above calculated interfacial free energy values agree with values calculated for Ni-based alloys. The lower interfacial free energy of L19 can be attributed partially to the interfacial segregation of Mo, which is estimated to reduce $\sigma_{\gamma/\gamma'}$ by about 1.6 mJ m^{-2} , and partially to a decrease in the lattice parameter misfit strain energy with increasing Ni-content [54,55], a parameter implicitly accounted for using the classical LSW model.

4. Summary and conclusions

Several Co-Al-(W)-based γ - γ' alloys, with 3–6 additional alloying elements, were investigated to combine recent results indicating significant increases in the γ' solvus temperature with additions of Ni, Ta, and Ti, and reduced mass density with the substitution of Mo and Nb for W. A maximum solvus temperature of 1167 ± 6 °C was achieved in an alloy with the composition Co-30Ni-7Al-4Ti-7W-1Ta, where no secondary phases were observed after 1000 h annealing at 900 °C, except for small amounts of the DO₁₉, χ -phase formed along grain boundary cracks near the edges of the sample because of local composition changes due to Al-loss by evaporation during the annealing process.

An alloy with the composition Co-30Ni-7Al-4Ti-3Mo-2W-1Nb-1Ta (L19) exhibited a promising combination of a high γ' volume

fraction ($\approx 65\%$), high γ' solvus temperature (1126 ± 2 °C), low density ($8.89 \pm 0.02 \text{ g cm}^{-3}$), and no secondary phase formation after prolonged aging at 900 °C (1000 h), 1000 °C (168 h), or 1100 °C (168 h). Atom-probe tomographic measurements of alloy L19 aged for 4 h at 900 °C demonstrated that Ni, Al, Ti, W, Nb, and Ta all partition preferentially to the γ' -precipitates while Co partitions strongly to the γ -matrix. The Mo concentration was found to be approximately equal in both the γ and γ' phases, but confined segregation of Mo to the γ/γ' heterophase interface was observed corresponding to a calculated total Gibbsian interfacial excess of $0.43 \pm 0.17 \text{ atoms} \cdot \text{nm}^3 \cdot \text{m}^{-2}$ and an integral reduction in the interfacial Gibbs free energy of $1.63 \pm 0.85 \text{ mJ m}^{-2}$.

In alloy L18, which had the same nominal composition as L19, but a reduced Ni content of 10%, only Co was observed to partition to the γ -matrix after 4 h aging at 900 °C, while Ni, Ti, Ta, Al, Nb, W, and Mo partitioned preferentially to the γ' -precipitates. Increasing the bulk Ni content from 10% to 30% resulted in enhanced partitioning of Ti and Al to the γ' -precipitates, and a corresponding reduction in the γ'/γ partitioning coefficient for Ta, W, Nb, Mo, and Co.

Analysis of the coarsening behavior at 900 °C of alloys L18 and L19, using the recent model of Philippe and Voorhees in conjunction with available Calphad thermodynamic and atomic mobility data, yield values of the interfacial Gibbs free energy of $35.0 \pm 18.6 \text{ mJ m}^{-2}$ and $29.2 \pm 15.5 \text{ mJ m}^{-2}$ for alloys L18 and L19, respectively, indicating that increasing the Ni content reduces the interfacial energy. This is potentially due to both the segregation of Mo to the γ/γ' interface and a reduction in lattice parameter misfit between the precipitate and matrix, and thus misfit strain energy, accompanying the increase in Ni concentration.

Acknowledgements

This work was performed in part under the financial assistance award 70NANB14H012 from U.S. Department of Commerce, National Institute of Standards and Technology as part of the Center for Hierarchical Materials Design (CHiMaD). Atom-probe tomography was performed at the Northwestern University Center for Atom-Probe Tomography (NUCAPT). The local-electrode atom-probe tomograph at NUCAPT was acquired and upgraded with equipment grants from the MRI program of the National Science Foundation (NSF DMR-0420532) and the DURIP program of the

Office of Naval Research (N00014-0400798, N00014-0610539, N00014-0910781). NUCAPT received support from the MRSEC program (NSF DMR-1121262) of the Materials Research Center, the SHyNE Resource (NSF NNCI-1542205), and the Initiative for Sustainability and Energy at Northwestern (ISEN).

References

- [1] C.S. Lee, Precipitation Hardening Characteristics of Ternary Cobalt-aluminum-x Alloys, Ph.D. dissertation, The University of Arizona, 1971.
- [2] J. Sato, T. Omori, K. Oikawa, I. Ohnuma, R. Kainuma, K. Ishida, Cobalt-based high-temperature alloys, *Science* 312 (2006) 90–91.
- [3] T.M. Pollock, J. Dibbern, M. Tsunekane, J. Zhu, A. Suzuki, New Co-based gamma-gamma prime high-temperature alloys, *JOM (J. Occup. Med.)* 62 (2010) 58–63.
- [4] N.L. Okamoto, T. Oohashi, H. Adachi, K. Kishida, H. Inui, P. Veyssi ere, Plastic deformation of polycrystals of $\text{Co}_3(\text{Al,W})$ with L_{12} structure, *Phil. Mag.* 91 (2011) 3667–3684.
- [5] K. Tanaka, M. Ooshima, N. Tsuno, A. Sato, H. Inui, Creep deformation of single crystals of new Co-Al-W-based alloys with fcc/ L_{12} two-phase microstructure, *Phil. Mag.* 92 (2012) 4011–4027.
- [6] L. Klein, A. Bauer, S. Neumeier, M. G oken, S. Virtanen, High temperature oxidation of γ/γ' -strengthened Co-based superalloys, *Corrosion Sci.* 53 (2011) 2027–2034.
- [7] H.-Y. Yan, V.A. Vorontsov, D. Dye, Effect of alloying on the oxidation behavior of Co-Al-W superalloys, *Corrosion Sci.* 83 (2014) 382–395.
- [8] F. Xue, H.J. Zhou, X.F. Ding, M.L. Wang, Q. Feng, Improved high temperature γ' stability of Co-Al-W alloys containing Ti and Ta, *Mater. Lett.* 112 (2013) 215–218.
- [9] F. Xue, H.J. Zhou, Q. Feng, Improved high-temperature stability and creep behavior property of novel Co-base single-crystal alloys containing Ta and Ti, *JOM (J. Occup. Med.)* 66 (2014) 2486–2494.
- [10] R.W. Jackson, M.S. Titus, M.R. Begley, T.M. Pollock, Thermal expansion behavior of new Co-based alloys and implications for coatings, *Surf. Coating Technol.* 289 (2016) 61–68.
- [11] H.J. Zhou, W.D. Li, F. Xue, L. Zhang, X.H. Qu, Q. Feng, Alloying effects on microstructural stability and γ' phase nano-hardness in Co-Al-W-Ta-Ta-base superalloys, *Superalloys 2016* (2016) 981–990.
- [12] E.A. Lass, Application of computational thermodynamics to the design of a Co-Ni-based γ' -strengthened superalloy, *Metall. Mater. Trans. A* 48A (2017) 2443–2459.
- [13] F. Pyczak, A. Bauer, M. G oken, U. Lorenz, S. Neumeier, M. Oehring, J. Paul, N. Schell, A. Schreyer, A. Stark, F. Symanzik, The effect of tungsten content on the properties of L_{12} -hardened Co-Al-W alloys, *J. Alloy. Comp.* 632 (2015) 110–115.
- [14] S.K. Makineni, B. Nithin, K. Chattopadhyay, Synthesis of a new tungsten free $\gamma-\gamma'$ cobalt-based superalloy by tuning alloying additions, *Acta Mater.* 85 (2015) 85–94.
- [15] S.K. Makineni, A. Samanta, T. Rohjirunsakool, T. Alam, B. Nithin, A.K. Singh, R. Banerjee, K. Chattopadhyay, A new class of high strength high temperature cobalt based $\gamma-\gamma'$ Co-Mo-Al alloys stabilized with Ta additions, *Acta Mater.* 97 (2015) 29–40.
- [16] M.S. Titus, A. Suzuki, T.M. Pollock, Creep and directional coarsening in single crystals of new $\gamma-\gamma'$ cobalt-based alloys, *Scripta Mater.* 66 (2012) 574–577.
- [17] H.-Y. Yan, V.A. Vorontsov, D. Dye, Alloying effects in polycrystalline γ' strengthened Co-Al-W base alloys, *Intermetallics* 48 (2014) 44–53.
- [18] S. Neumeier, L.P. Freund, M. G oken, Novel wrought γ/γ' cobalt base superalloys with high strength and improved oxidation resistance, *Scripta Mater.* 109 (2015) 104–117.
- [19] D.J. Larson, T.J. Prosa, R.M. Ulfing, B.P. Geiser, T.F. Kelly, *Local Electrode Atom Probe Tomography*, Springer, New York, 2013.
- [20] M.K. Miller, E.A. Kenik, Atom probe tomography: a technique for nanoscale characterization, *Microsc. Microanal.* 10 (2004) 336–341.
- [21] O.C. Hellman, J.A. Vandenbroucke, J. R using, D. Isheim, D.N. Seidman, Analysis of three-dimensional atom-probe data by the proximity histogram, *Microsc. Microanal.* 6 (2000) 437–444.
- [22] O.C. Hellman, D.N. Seidman, Measurement of the Gibbsian interfacial excess of solute at an interface of arbitrary geometry using three-dimensional atom probe microscopy, *Mater. Sci. and Eng. A* 327 (2002) 24–28.
- [23] J. Coakley, E.A. Lass, D. Ma, M. Frost, D.N. Seidman, D.C. Dunand, H.J. Stone, Rafting and elastoplastic deformation of superalloys studied by neutron diffraction, *Scripta Mater.* 134 (2017) 110–114.
- [24] ASM Handbook, in: H. Baker, H. Okamoto (Eds.), Volume 03-Alloy Phase Diagrams, ASM International, 1992.
- [25] S.K. Makineni, B. Nithin, D. Palanisamy, K. Chattopadhyay, Phase evolution and crystallography of precipitates during decomposition of new “tungsten-free” Co(Ni)-Mo-Al-Nb $\gamma-\gamma'$ superalloys at elevated temperatures, *J. Mater. Sci.* 51 (2016) 7843–7860.
- [26] R.C. Reed, *The Superalloys: Fundamentals and Applications*, Cambridge University Press, 2006.
- [27] E.A. Lass, M.E. Williams, C.E. Campbell, K.-W. Moon, U.R. Kattner, Phase stability and phase equilibrium in ternary Co-Al-W at 900 °C, *J. Phase Equilibria Diffusion* 35 (2014) 711–723.
- [28] E.A. Lass, R.D. Grist, M.E. Williams, Phase equilibria and microstructural evolution in ternary Co-Al-W between 750 °C and 1100 °C, *J. Phase Equilibria Diffusion* 37 (2016) 387–401.
- [29] K. Shinagawa, T. Omori, J. Sato, K. Oikawa, I. Ohnuma, R. Kainuma, K. Ishida, Phase equilibria and microstructure of γ' in the Co-Ni-Al-W system, *Mater. Trans.* 49 (2008) 1474–1479.
- [30] S. Meher, H.Y. Yan, S. Nag, D. Dye, R. Banerjee, Solute partitioning and site preference in γ/γ' cobalt-base alloys, *Scripta Mater.* 67 (2012) 850–853.
- [31] P.J. Bocchini, E.A. Lass, K.-W. Moon, M.E. Williams, C.E. Campbell, U.R. Kattner, D.C. Dunand, D.N. Seidman, Atom-probe tomographic study of γ/γ' interfaces and compositions in an aged Co-Al-W superalloy, *Scripta Mater.* 68 (2013) 563–566.
- [32] S. Meher, R. Banerjee, Partitioning and site occupancy of Ta and Mo in Co-base γ/γ' alloys studied by atom probe tomography, *Intermetallics* 49 (2014) 138–142.
- [33] S. Meher, L.J. Carroll, T.M. Pollock, Solute partitioning in multi-component γ/γ' Co-Ni-base superalloys with near-zero lattice misfit, *Scripta Mater.* 113 (2016) 185–189.
- [34] I. Blum, S.-I. Baik, M.G. Kanatzidis, D.N. Seidman, An integral method for the calculation of the reduction in interfacial free energy due to interfacial segregation, unpublished results.
- [35] Z. Mao, C. Booth-Morrison, C.K. Sudbrack, G. Martin, D.N. Seidman, Kinetic pathways for phase separation: an atomic-scale study in Ni-Al-Cr alloys, *Acta Mater.* 60 (2012) 1871–1888.
- [36] Z. Mao, C.K. Sudbrack, K.E. Yoon, G. Martin, D.N. Seidman, The mechanism of morphogenesis in a phase-separating concentrated multicomponent alloy, *Nature Mater.* 6 (2007) 210–216.
- [37] I.M. Lifshitz, V.V. Slyozov, The kinetics of precipitation of supersaturated solid solutions, *J. Phys. Chem. Solid.* 19 (1961) 35–50.
- [38] C. Wagner, The theory of aging precipitates by dissolution-precipitation (Ostwald ripening), *Z. Elektrochem.* 65 (1961) 581–591.
- [39] OriginLab: Origin Online Help, Theory of nonlinear curve fitting, <http://www.originlab.com/doc/Origin-Help/NLFit-Theory>, accessed: May 31, 2017.
- [40] A. Baldan, Progress in Ostwald ripening theories and their applications to nickel-base superalloys, Part I: ostwald ripening theories, *J. Mater. Sci.* 37 (2002) 2171–2202.
- [41] D.J. Chellman, A.J. Ardell, The coarsening of γ' precipitates at large volume fractions, *Acta Metall.* 22 (1974) 577–588.
- [42] A.D. Brailsford, P. Wynblatt, The dependence of Ostwald ripening kinetics on particle volume fraction, *Acta Metall.* 27 (1979) 489–497.
- [43] H.A. Calderon, P.W. Voorhees, J.L. Murray, G. Kostorz, Ostwald ripening in concentrated alloys, *Acta Metall. Mater.* 42 (1994) 991–1000.
- [44] J.E. Morral, G.R. Purdy, Particle coarsening in binary and multicomponent alloys, *Scripta Metall. Mater.* 30 (1994) 905–908.
- [45] C.J. Kuehmann, P.W. Voorhees, Ostwald ripening in ternary alloys, *Metall. Mater. Trans. A* 27A (1996) 937–943.
- [46] A. Umantsev, G.B. Olson, Ostwald ripening in multicomponent alloys, *Scripta Metall. Mater.* 29 (1993) 1135–1140.
- [47] T. Philippe, P.W. Voorhees, Ostwald ripening in multicomponent alloys, *Acta Mater.* 61 (2013) 3244–3237.
- [48] X.-G. Lu, M. Selleby, B. Sundman, Assessments of molar volume and thermal expansion for selected bcc, fcc, and hcp metallic elements, *Calphad* 29 (2005) 68–89.
- [49] C.E. Campbell, W.J. Boettinger, U.R. Kattner, Development of a diffusion mobility database of Ni-base superalloys, *Acta Mater.* 50 (2002) 775–792.
- [50] Thermocalc version 2015b, Thermo-Calc Software AB, Stockholm, Sweden, 2015.
- [51] J.-O. Andersson, J.  gren, Models for numerical treatment of multicomponent diffusion in simple phases, *J. Appl. Phys.* 72 (1992) 1350–1355.
- [52] C.E. Campbell, A New Technique for Evaluating Diffusion Mobility Parameters, Proceeding of the 1st International Conference on Diffusion in Solids and Liquids-DSL2005, University of Aveiro, Aveiro, Portugal, July 6–8, 2005.
- [53] C.E. Campbell, A.L. Rukhin, Evaluation of self-diffusion data using weighted means statistics, *Acta Mater.* 59 (2011) 5194–5201.
- [54] C.K. Sudbrack, R.D. Noebe, D.N. Seidman, Compositional pathways and capillary effects during isothermal precipitation in a nondilute Ni-Al-Cr alloy, *Acta Mater.* 55 (2007) 119–130.
- [55] C.H. Zenk, S. Neumeier, N.M. Engl, S.G. Fries, O. Dolotko, M. Weiser, S. Virtanen, M. G oken, Intermediate Co/Ni-base model superalloys-therophysical properties, creep and oxidation, *Scripta Mater.* 112 (2016) 83–86.